A spectral study of the black hole X-ray binary MAXI J1820+070 with *AstroSat* and *NuSTAR*

Sudip Chakraborty [ORCID],[1]⋆ Nilam Navale,[2,3] Ajay Ratheesh[4,5,6] and Sudip Bhattacharyya [ORCID][1]

[1]*Department of Astronomy and Astrophysics, Tata Institute of Fundamental Research, Mumbai 400005, India*
[2]*University Department of Physics, University of Mumbai, Kalina, Santacruz, Mumbai 400098, India*
[3]*Ramniranjan Jhunjhunwala College, Ghatkopar, Mumbai 400086, India*
[4]*Department of Physics, University of Rome 'Tor Vergata', via della Ricerca Scientifica 1, I-00133 Rome, Italy*
[5]*INAF-IAPS, Via del Fosso del Cavaliere 100, I-00133 Rome, Italy*
[6]*Department of Physics, University of Rome 'La Sapienza', P. le A. Moro 2, I-00185 Rome, Italy*

ABSTRACT

MAXI J1820+070 is a newly discovered transient black hole X-ray binary, which showed several spectral and temporal features. In this work, we analyse the broad-band X-ray spectra from all three simultaneously observing X-ray instruments onboard *AstroSat*, as well as contemporaneous X-ray spectra from *NuSTAR*, observed during the hard state of MAXI J1820+070 in 2018 March. Implementing a combination of multicolour disc model, relativistic blurred reflection model RELXILLLPCP, and a distant reflection in the form of XILLVERCP, we achieve reasonable and consistent fits for *AstroSat* and *NuSTAR* spectra. The best-fitting model suggests a low temperature disc ($kT_{in} \sim 0.3$ keV), iron overabundance ($A_{Fe} \sim 4$–5 solar), a short lamp-post corona height ($h \lesssim 8R_g$), and a high corona temperature ($kT_e \sim 115$–150 keV). Addition of a second Comptonization component leads to a significantly better fit, with the kT_e of the second Comptonization component being ~ 14–18 keV. Our results from independent observations with two different satellites in a similar source state indicate an inhomogeneous corona, with decreasing temperature attributed to increasing height. Besides, utilizing the broader energy coverage of *AstroSat*, we estimate the black hole mass to be 6.7–$13.9\,M_\odot$, consistent with independent measurements reported in the literature.

Key words: accretion, accretion discs – methods: data analysis – X-rays: binaries – X-rays: individual: MAXI J1820+070.

1 INTRODUCTION

Accreting black hole X-ray binaries are unique astrophysical laboratories to probe matter in extreme conditions. Based on the mass of the companion star, they can be classified into High Mass X-ray Binary (HMXB) and Low Mass X-ray Binary (LMXB). In black hole LMXBs, the main source of power is the gravitational energy released by matter accreted from the companion low mass star on to the black hole via Roche lobe overflow (e.g. Frank, King & Raine 2002). Based on the long-term temporal evolution of the X-ray emission, LMXBs can be further categorized into persistent and transient sources. Almost all black hole LMXBs are transients (Done, Gierliński & Kubota 2007). The transient LMXBs can be in a quiescent state for a long time, probably undetected until they go into outbursts increasing intensities by few orders of magnitude. They exhibit various source states, such as Low Hard State (LHS), High Soft State (HSS), and High Intermediate state (HIS), which can be identified from the hardness intensity diagram (HID) (Belloni et al. 2000; Remillard & McClintock 2006). The changes in the spectral states could be attributed to the change in the geometry of the accretion disc (Remillard & McClintock 2006).

In terms of the X-ray spectrum, the HSS is dominated by a multicolour black-body emission, attributed to the accretion disc. This is interpreted as the disc being very close to the innermost circular stable orbit (ISCO), leading to high disc temperatures (Belloni et al. 2000; Remillard & McClintock 2006). On the other hand, the LHS is mainly dominated by a variable power-law component, with some hint of low-temperature disc component. The lower disc temperature is interpreted as the disc being truncated at a much larger radius (see, however, Reis, Fabian & Miller 2010). The power-law component is generally attributed to a spatially compact region located above the central region of the accretion disc, named 'corona' (Reynolds 2014). In this scenario, the hot corona irradiates the accretion disc, producing fluorescent and backscattered radiation. The re-emission from the irradiated disc is thought to be the (thermal) soft excess ~ 1 keV, broad iron line complex, and Compton hump around ~ 30 keV (Fabian 2016). In LHS, the Comptonizing corona and the reflection from the disc give rise to the power-law continuum and reflection features, respectively. While in HSS, the corona weakens or disappears. Thus, LHS is dominated by power-law emission, whereas the HSS is dominated by the higher temperature disc emission. This interpretation of states and state transitions as changes in accretion disc geometry is being challenged in recent years. For example, Kara et al. (2019) have proposed the idea of contracting corona as opposed to changing disc truncation radius, as an explanation of states and state transitions. The exact geometry

⋆ E-mail: sudip.chakraborty@tifr.res.in

of the corona is still unclear. While a lamp-post geometry is often used for computational simplicity, this may not sufficiently reflect the actual scenario (Chauvin et al. 2018). Finally, Yamada et al. (2013), Basak et al. (2017) have proposed more general, inhomogeneous structure of the corona.

MAXI J1820+070 is a recently discovered bright X-ray transient, detected with Monitor of All-sky X-ray image, or *MAXI* (Matsuoka et al. 2009) on board the International Space Station (ISS) on 2018 March 11 at 12:50 UT (Kawamuro et al. 2018). Its optical counterpart, named ASSASN-2018ey, was observed with All-Sky Automated Survey for SuperNovae (ASAS-SN) (Denisenko 2018; Tucker et al. 2018). A consecutive *Swift* /BAT trigger led to a follow up monitoring of the source with XRT, which located the X-ray source at RA (J2000) = +18h 20m 21.88s and Dec (J2000) = +07d 11m 08.3s with an uncertainty of 1.5 arcsec (Kennea 2018).

During its 2018 outburst, the object was subsequently observed in multiple wavelengths: from radio (Bright, Fender & Motta 2018; Trushkin et al. 2018), to infrared (Casella et al. 2018; Mandal et al. 2018), to optical (Baglio, Russell & Lewis 2018; Bahramian, Strader & Dage 2018; Gandhi et al. 2018; Garnavich & Littlefield 2018; Littlefield 2018; Sako et al. 2018). Optical observations (Baglio, Russell & Lewis 2018) along with hard X-ray power-law spectrum, and large amplitude in the broad-band power spectrum (Uttley et al. 2018) suggested that the source is a Black Hole Low mass X-ray Binary (BH LMXB). After the beginning of the outburst, MAXI J1820+070 underwent rapid increase in flux in both soft and hard X-rays, with hardness ratio remaining more or less constant (Del Santo & Segreto 2018). Subsequent optical observations revealed an optical period of ∼3.4 h (Richmond 2018), as well as correlations between X-ray and optical brightness (Paice et al. 2018, 2019; Townsend et al. 2018; Yu et al. 2018). Further sub-millimetre detection (Tetarenko et al. 2018) and flat radio spectrum (Tetarenko et al. 2018) hinted the launch of a relativistic jet. After the initial rise in intensity, MAXI J1820+070 underwent a slow decay from around MJD 58200. The hard X-ray flux dropped sharply around MJD 53805, causing a state transition to the soft state. The source remained in the soft state for around 60 d before transiting back to the hard state around MJD 58390, before fading away into quiescence after MJD 58400 (Fig. 1).

During the LHS, MAXI J1820+070 had a hard spectrum with a photon index of ∼1.5 (Del Santo & Segreto 2018). Low-frequency quasi-periodic oscillations (QPOs) were detected in Optical and X-ray wavelengths (10–50 mHz) (Gandhi et al. 2018; Mereminskiy et al. 2018; Yu et al. 2018). Strong optical and X-ray short-term variabilities on time-scales of less than 1 s were also reported (Gandhi et al. 2018; Sako et al. 2018). Kara et al. (2019) performed spectrotemporal study of MAXI J1820+070 and detected reverberation time lags between 0.1–1.0 and 1.0–10.0 keV energy bands. The authors have observed a corona height $<5R_g$ and an inner disc radius $<2R_g$ (where R_g is the gravitational radius of the black hole, defined as $R_g = GM/c^2$). They also claimed that with the evolution of the outburst the corona became compact and shifted close to the compact object. Spectral analysis during the LHS by Buisson et al. (2019) not only supported this claim but also suggested a correlation between X-ray luminosity and coronal temperature. However, a general relativistic simulation using the spectral analysis indicated that the spectral softening was due to the change in the inner disc radius rather than the coronal geometry (Roh 2020). The mass function of the binary system was reported to be $5.18 \pm 0.15\,M_\odot$ (Torres et al. 2019). By constraining the inclination angle to be 69° $< i < 77°$, the black hole mass was estimated to be 7–8 $M_\odot$ (Torres et al. 2019). Using radio parallax method, Atri et al. (2020) estimated
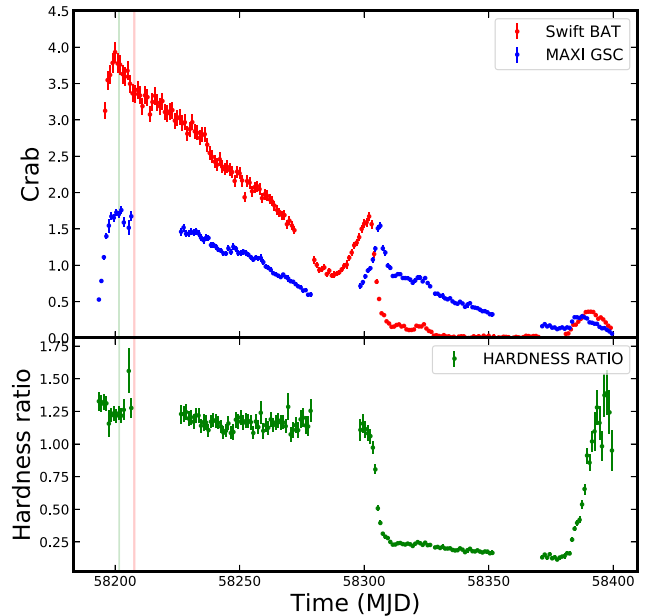

Figure 1. Upper panel: The red and blue points show the Crab normalized light curve of MAXI J1820+070 obtained using *Swift* /BAT and *MAXI*/GSC in energy range 15–50 and 4–10 keV. Lower panel: Crab normalized Hardness ratio (4–10 keV/2–4 keV) obtained using *MAXI*/GSC. The red and green vertical bands mark the epochs observed with *AstroSat* and *NuSTAR* , respectively.

Table 1. *NuSTAR* and *AstroSat* observation details. In case of *NuSTAR*, we have mentioned only the FPMA exposure time. In case of *AstroSat* , we have mentioned only the SXT exposure time. The LAXPC and CZTI exposure times are higher by more than a factor of 2.

Instrument	Obs ID	Obs. date (yyyy-mm-dd)	Exposure (s)
NuSTAR	90401309010	2018-03-24/25	2660
AstroSat	9000001994	2018-03-30/31	11 768

the accurate distance to the source to be $2.96 \pm 0.33\,kpc$, further constraining the black hole mass of the source to $9.2 \pm 1.3\,M_\odot$. Analysing the HSS spectra, Fabian et al. (2020) found the black hole mass to be ∼7–8 $M_\odot$, and the black hole spin to be moderately low (dimensionless spin parameter, *a*, between −0.5 and +0.5). Using DR2 data of *Gaia*, Gandhi et al. (2019) found the source distance to be $3.46^{+2.18}_{-1.03}$ kpc. By analysing the soft X-ray data from NICER during the rising phase of outburst, Uttley et al. (2018) found the Galactic extinction (N_H) to be 1.5×10^{21} cm^{-2}.

In this work, we investigate the broad-band spectral characteristics of the hard state spectra of MAXI J1820+070 during its 2018 outburst. We use the data from *AstroSat* observation during 2018 March 30–31 and a suitably chosen *NuSTAR* observation during 2018 March 24–25 (see Table 1 for details of the observations). The *AstroSat* spectra (without the Cadmium Zinc Telluride Imager (CZTI)) were presented with a simple model fit (and with greater systematic uncertainty assumed) in Mudambi et al. (2020). Of the broad-band X-ray satellites currently available, *NuSTAR* and *AstroSat* provide good energy resolution in hard X-ray range (>10 keV), with *AstroSat* covering a broader energy range. Here we utilize this opportunity, to systematically and uniformly study the broad-band spectra of this BHXB from these independent satellite instruments

using detailed spectral models for the first time. The paper is organized as follows. In Section 2 we describe the data reduction procedure of *NuSTAR* , as well as all three pointing X-ray instruments on board *AstroSat* , namely Soft X-ray Telescope (SXT), The Large Area X-ray Proportional Counter (LAXPC), and CZTI. In Section 2.5, we describe the *MAXI*/GSC and *Swift* /BAT light curves and HID generation. We then describe the states and state transition, as well as the *NuSTAR* data selection based on the mentioned HID in Section 2.6. Furthermore, we present an in-depth spectral analysis of *NuSTAR* and *AstroSat* data in Sections 3.2.1 and 3.2.2, followed by an estimation of the black hole mass based on the same spectral fit in Section 3.2.3. Finally, we summarize our results and discuss their implications in Section 4.

2 OBSERVATION AND DATA REDUCTION

AstroSat , the first Indian dedicated astronomy satellite, was successfully launched on 2015 September 28, carrying five scientific instruments on board (Singh et al. 2014): the focusing Soft X-ray Telescope (SXT), Large Area X-ray Proportional Counters (LAXPCs, 3 units), the hard X-ray CZTI, the all-sky monitor called Scanning Sky Monitor (SSM) ,and the Ultraviolet Imaging Telescopes (UVIT). *AstroSat* observed MAXI J1820+070 in a hard state during the outburst on 2018 March 30–31, and we use the data from all three X-ray instruments (SXT, LAXPC, and CZTI) in this work.

2.1 SXT

SXT (Singh et al. 2016; Singh et al. 2017) is a grazing incidence X-ray telescope on board *AstroSat* , with a focal length of 2 m. It covers the energy range of 0.3–8 keV and has a field of view of ∼40 arcmin (Singh et al. 2014).

The SXT data are acquired in the PC mode and is significantly piled up. To minimize the effect of the pile-up, source spectrum is extracted from an annulus between 6 and 15 arcmin from the centre of the image (the details of the region selection for avoiding pile-up, are described in Appendix A). The deep blank sky background spectrum, provided by the instrument team,[1] is used for the spectral modelling.

2.2 LAXPC

LAXPC (Yadav et al. 2016) is a proportional counter array on board *AstroSat* (Agrawal 2006; Singh et al. 2014) with a large effective area, which observes sources in Event Analysis (EA) mode with absolute time resolution of 10 µs in the energy range of 3.0–80.0 keV. The extraction of light curve and spectrum from level 1 data is done by LAXPCSOFTV3.1[2] along with background light curve and background spectrum. Among the three units of LAXPC, we have considered only one unit. As LAXPC30 has gain instability issue caused by a gas leakage and LAXPC10 was showing unpredictable HV variations, the results reported in this paper are from LAXPC20. We have also extracted light curves in different energy bands corresponding to *NuSTAR* , *Swift* /BAT, and *MAXI*/GSC energies to plot HID as shown in Fig. 2.
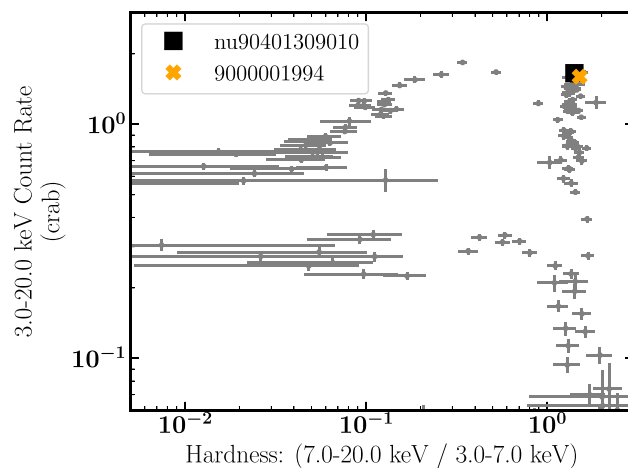
Figure 2. Hardness intensity diagram (HID) of MAXI J1820+070 with 1 d averaged *MAXI*/GSC monitoring observations during its first outburst. The scattered grey circles indicate the overall evolution of the source from MJD 58188 to MJD 58734. The *AstroSat* observation of interest is marked with an orange cross on the HID and the nearest *NuSTAR* observation which have consistent spectral properties is marked with a black square. The size of the error bars is similar to that of marker size for these two observations. See Section 3.1 for a discussion on the HID.

2.3 CZTI

The level 1 data of *AstroSat* CZTI is reduced to level 2 cleaned events, spectra, and light curve using the tool CZTIPIPELINE of CZTIPIPELINE Ver 2.1.[3] The total light curve before background reduction is then checked for any instrumental anomalies near the South Atlantic Anomaly (SAA). The time intervals very close to the SAA, where a sharp increase in the count-rate is observed, are excluded. Only Quadrant 0 in CZTI is used for the spectrum, as the instrumental response features in the other quadrants are yet to be understood. Further, module 13 in Quadrant zero is excluded as with Lower Limit of Detection (LLD) at around 50 keV, it does not span the entire spectral region of interest from the CZTI in this particular case.

2.4 *NuSTAR*

MAXI J1820+070 was observed with *NuSTAR* (Harrison et al. 2013) during 2018 March 24–25 (the reasons of this data selection are detailed in Section 3.1 and Section 4). The *NuSTAR* data are processed using v.1.8.0 of the NUSTARDAS pipeline with *NuSTAR* CALDB v220171002. After filtering background flares due to enhanced solar activity by setting saacalc = 2, saamode = OPTIMIZED, and tentacle = no in NUPIPELINE, the effective exposure times are 2.6 and 2.8 ks for the two focal plane modules FPMA and FPMB, respectively. The source spectra are extracted from a circular region of the radius 180 arcsec centred on the source location. The background spectra are extracted from a blank region on the detector furthest from the source location to avoid source photons. The spectra are grouped in *isis* (Houck & Denicola 2000) version 1.6.2–41 to have a signal-to-noise ratio of at least 50 per bin, similar to Buisson et al. (2019).

2.5 *MAXI*/GSC and *Swift*/BAT light curve

The Burst Alert Telescope on board Neil Gehrels *Swift* Observatory (*Swift*/BAT) and Gas Slit Camera on board Monitor of All-sky X-ray Image (*MAXI*/GSC) continuously traced the source throughout the outburst phase. The daily averaged light curves from *Swift*/BAT in 15 to 50 keV have been obtained from https://swift.gsfc.nasa.gov/results/transients/ and is normalized by the Crab count-rate in *Swift*/BAT. A very sharp increase in flux is seen during the initial phase with a gradual decrease. Another peak is also seen around MJD 58300. For *MAXI*/GSC, http://maxi.riken.jp provided the light curves in 2–4 and 4–10 keV. The light curves are further normalized in respective bands by the Crab count-rate in *MAXI*/GSC. Further the hardness ratios are also obtained using the Crab normalized count rates, the hard band being 4–10 keV and soft being 2–4 keV. A sharp rise is seen also in the *MAXI*/GSC (4–10 keV) during the initial phase but the hardness ratio remains constant. A sharp decrease is also observed around MJD 58300, and a further sharp rise is observed around MJD 58380. *AstroSat* and *NuSTAR* made pointed observations during the outburst marked by red and green vertical bands.

2.6 Hardness intensity diagram generation from *MAXI*

The HID for MAXI J1820+070 is been generated using daily monitoring data from *MAXI*/GSC (Fig. 2). For hardness ratio (defined as the background-subtracted count-rate ratio in quoted energy bands), we choose 3.0–7.0 and 7.0–20.0 keV energy bands and consider intensity from 3.0 to 20.0 keV. Each point in the HID is averaged over 1 d. The pointed observations of the *AstroSat* (orange cross) and the *NuSTAR* (black square) reported in this paper are marked over the HID. The data from all three instruments are normalized by Crab counts, for a better comparison.

3 RESULTS

3.1 Spectral state and transition

Most of the black hole X-ray binaries (BHXBs) are of transient nature and are discovered when outbursts occur. The evolution of an outburst in a BHXB is well depicted by a HID (Homan et al. 2001; Homan & Belloni 2005; Remillard & McClintock 2006; Fender, Homan & Belloni 2009), which traces a 'q-shaped' trajectory moving in the counter-clockwise direction. The best-known example is GX 339-4, which undergoes recurrent outbursts and has always followed a 'q' shaped path on HID (Belloni et al. 2005; Fender et al. 2009; Motta et al. 2011). The HID is a model-independent tool to study the state transitions in such BHXBs.

We generate the HID for MAXI J1820+070 (Fig. 2), using a daily monitoring *MAXI*/GSC data since the time of its discovery. The source has followed a 'q'-shaped track similar to GX 339-4. Various states on HID, as described in Section 1, are evident in Fig. 2. We plot the *AstroSat* observation of our interest over the HID (orange cross), which is found to be in the hard state. During this state both hardness and intensity are high. We also considered one of the nearest *NuSTAR* observations (black square). The *NuSTAR* observation is also in a similar source hardness.

3.2 Spectral analysis

The RMF files for SXT and LAXPC are obtained from the respective Payload Operation Centre (POC) websites.[45] For SXT, sxt_pc_mat_g0to12.rmf is used as the RMF and sxt_pc_excl00_v04_20190608.arf is used as the ARF, whereas for LAXPC20 the response file lx20cshm03v1.0.rmf is used. For joint fitting, both the SXT and LAXPC spectral files are binned in GRPPHA to have at least 30 counts per bin to facilitate χ^2 fitting. A 2 per cent systematic uncertainty, as prescribed by the instrument teams,[6] is used for the spectral fitting. For CZTI, the spectral and response files are generated using CZTBINDATA and CZTRSPGEN of the CZTIPIPELINE,[7] respectively.

The spectral fitting and statistical analysis are carried out using the XSPEC version v-12.9.0n (Arnaud 1996). Energy ranges of 1.3–7.0 and 5–60 keV are used for SXT and LAXPC20, respectively. The photons below 1.3 keV and above 7.0 keV for SXT, and below 5.0 keV and above 60 keV for LAXPC, are ignored to avoid larger systematic errors. For CZTI, the energy range of 30 to 120 keV is used. Additionally, a gain correction is applied to the SXT data using the XSPEC command 'gain fit' with a slope of unity. The best-fitting offset value is found to be 34 eV and is used throughout the paper. For the joint fitting between different *AstroSat* instruments, a cross-normalization constant (implemented using CONSTANT model in XSPEC) is allowed to vary freely for LAXPC and CZTI and is assumed to be unity for SXT. Similar cross-normalization is considered between FPMA and FPMB for *NuSTAR* data fit. For *NuSTAR*, an energy range between 3 and 78 keV is considered for spectral fitting. To avoid the sharp instrumental features (as reported by Xu et al. 2018), energies between 11–12 and 23–28 keV are excluded (Buisson et al. 2019). All the models, as described below, include the Galactic absorption through the implementation of the TBABS model. The corresponding abundances are set in accordance with the Wilms, Allen & McCray (2000) photoelectric cross-sections. The neutral hydrogen column density (N_H) is fixed to 1.5×10^{21} cm^{-2} (Uttley et al. 2018) for all the described models. All parameter uncertainties are reported at the 90 per cent confidence level for one parameter of interest.

3.2.1 Spectral fits without reflection

First of all, to demonstrate the reflection features, we fit the *NuSTAR* spectra with an absorbed cutoff power-law model, TBABS×CUTOFFPL in XSPEC notation. For this, we only consider the energy intervals of 3–4, 8–12, and 40–78 keV, where reflection from the disc has minimal effect. As displayed in the second panel of Fig. 3, a broad iron Fe K-α emission with a narrow core, as well as a Compton hump peaking around 30 keV, are evident in the residuals. The slight difference (∼1 per cent) between FPMA and FPMB below 5 keV, is within the calibration accuracy of *NuSTAR* (Madsen et al. 2015).

For a better explanation of the observed broad-band energy spectra, we fit the *NuSTAR* data with a model comprising of a combination of multicoloured disc black-body (discbb: Mitsuda et al. 1984; Makishima et al. 1986) and thermal Comptonization (NTHCOMP: Zdziarski; Johnson & Magdziarz 1996; Życki, Done & Smith 1999),
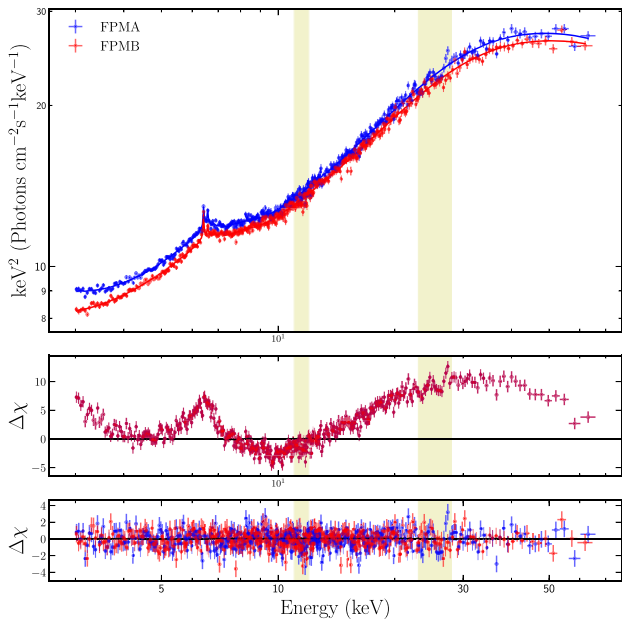

Figure 3. Results of 3–78 keV *NuSTAR* spectral fit of MAXI J1820+070 (see sections 3.2.2, 4 for further details). Top panel: the unfolded *NuSTAR* spectra. The blue and red points indicate FPMA and FPMB data, respectively. The spectra are folded with M2 model here. The yellow vertical bands denote the energy ranges ignored for spectral fitting due to instrumental features. Middle panel: The residuals of *NuSTAR* data, fitted with a fiducial TBABS×CUTOFFPL model. A soft excess, broad iron line and a Compton hump around ∼30 keV are visible. Bottom panel: Residuals from M2 model fit.

TBABS×(DISKBB + NTHCOMP) in XSPEC notations. The seed photon temperature in NTHCOMP is set to the innermost temperature (T_{in}) of the DISKBB component. In the energy range mentioned before, we get the best-fitting DISKBB T_{in} to be $0.77^{0.06}_{-0.05}$ keV, a power-law index (Γ) of 1.58 ± 0.01, and the electron temperature kT_e to be 19.2 ± 0.3 keV. The fit results in a reduced χ^2/dof of 404.2/211. The value of the cross-normalization factor between FPMA and FPMB is found to be 0.96 ± 0.01 (∼4 per cent), which is within the accepted limit of ≤ 5 per cent (Madsen et al. 2015; Marcotulli et al. 2017). Due to the limited spectral coverage assumed here, the value of kT_e is somewhat low. To get a better fit and to explore the possibility of additional spectral components, we add another NTHCOMP model to the existing model. This double Comptonization model gives a much better fit, with a χ^2/dof of 227.8/208. The fit results in a segregation of corona temperatures, with the best-fitting kT_e being $27.4^{2.7}_{-2.3}$ and $1.35^{0.02}_{-0.05}$ keV. The T_{in} of the disc is found to be 0.42 ± 0.01 keV. Note that this exercise is for a demonstration purpose only and the derived values are unreliable/unphysical as these fits within narrow energy bands do not include the effect of reflection, which we will discuss in greater depth in Section 3.2.2. In fact, the second Comptonization component in this model could be fitting for the Compton hump of the reflection (though we have tried to avoid this by ignoring the corresponding energy range) rather than a true second Comptonization. This shows the need for proper reflection modellings. Nevertheless, the important qualitative indication from this exercise is the possible existence of a second Comptonization component, with a lower corona temperature.

Inspired by this result, we investigate the possibility of a double Comptonization scenario in greater detail in Section 3.2.2. Until now, we have not explored the reflection. In the following section,

we perform an in-depth reflection modelling of both the *NuSTAR* and *AstroSat* broad-band spectra.

3.2.2 Spectral fits with reflection

For a detailed investigation of the broad-band spectra including the reflection features, we use the self-consistent relativistic disc reflection models from RELXILL model suite (relxill v1.2.0: Dauser et al. 2014; García et al. 2014). To minimize the number of free parameters, we assume a lamp-post geometry of the Comptonizing corona and use the model RELXILLLPCP which internally includes an NTHCOMP continuum. However, we only include the reflected flux from the RELXILLLPCP component (by setting the model parameter refl_frac<0). We add an explicit NTHCOMP component to represent the continuum. The seed photon temperature of the NTHCOMP component is tied to the inner accretion disc temperature (DISKBB T_{in}), and the electron temperatures (kT_e) and spectral indices (Γ) of both the NTHCOMP and RELXILLLPCP components are tied together. As before, the value of N_H is fixed to 1.5×10^{21} cm^{-2}, and the T_{in} from the additional DISKBB component is used as the seed temperature for the internal NTHCOMP continuum.

The inner radius (R_{in}) of the thin accretion disc, and the dimensionless black hole spin parameter (a), which are reflection spectrum parameters, are degenerate. For simplicity in spectral fitting, we assume a maximally spinning black hole ($a = 0.998$), and fit for R_{in} (for further discussion, refer to section 4). We fix the outer edge of the accretion disc (R_{out}) at $400R_g$ (where R_g is the gravitational radius of the black hole, defined as $R_g = GM/c^2$). On the other hand, we keep the inclination angle free (the data has sufficient signal for this purpose, as shown by Buisson et al. 2019). The reflection fraction can thus be self-consistently determined by fitting R_{in} and the height of the lamp-post (h) from ray-tracing calculations (Dauser et al. 2014). To account for the narrow core of the Fe-Kα line, we use the unblurred reflection model XILLVERCP (García & Kallman 2010). Similar to our implementation of RELXILLLPCP, we use XILLVERCP only as a reflection component. The refl_frac of XILLVERCP is fixed at -1, as only insignificant variations are found in the subsequent fits if the refl_frac is allowed to vary freely. We tie the Γ and kT_e of the input continuum, as well as the iron abundances (A_{Fe}) and inclination angles (θ) of the RELXILLLPCP and the XILLVERCP components. The ionization parameters ($\xi = L/nR^2$, where L is the ionizing continuum luminosity, R is the distance to the ionizing source, and n is the gas density) are allowed to be free for both the components. For XILLVERCP, we allow the logξ to be non-zero, thus allowing for distant reprocessing by ionized gas. Thus, the total model setup is TBabs×(diskbb+Nthcomp(1)+relxilllpCp(1) +xillverCp). This becomes our model M1 in Table 2.

Inspired by the two Comptonization scenario presented in Section 3.2.2, we further add an additional NTHCOMP to the M1 model, reflected through the XILLVERCP component. For this purpose, we link the Γ and kT_e between the XILLVERCP and the new NTHCOMP components. The seed temperature of the new NTHCOMP is again linked to the T_{in} of the DISKBB. Thus, the resulting model TBabs×(diskbb+Nthcomp(1)+relxilllpCp(1) +xillverCp+Nthcomp(2)) becomes our model M2 in Table 2.

To summarize, the two main models (in Table 2) considered in our works are as follows:

(i) TBabs× (diskbb+Nthcomp(1)+relxilllpCp(1) +xillverCp): This forms the M1 model in Table 2. Here, the NTHCOMP acts as the continuum, and the RELXILLLPCP and XILLVERCP

Table 2. Parameters of fits to MAXI J1820+070 spectra in the hard state observations with *AstroSat* and *NuSTAR* . The models M1, M2, and M3 are detailed in section 3.2.2. Errors represent 90 per cent confidence intervals. ^{f} denotes that the corresponding parameter is frozen. ^{p} or $_p$ denotes that the parameter is pegged at the upper/lower limit value.

Spectral component	Parameter	*NuSTAR* M1	*NuSTAR* M2	*AstroSat* M1	*AstroSat* M2	*AstroSat* M3
diskbb	kT_{in} (keV)	$0.44^{+0.08}_{-0.07}$ (FPMA) $0.42^{+0.09}_{-0.08}$ (FPMB)	$0.45^{+0.06}_{-0.05}$ (FPMA) $0.43^{+0.05}_{-0.05}$ (FPMB)	$0.33^{+0.01}_{-0.01}$	$0.31^{+0.01}_{-0.01}$	$0.35^{+0.01}_{-0.01}$
	norm ($\times 10^4$)	$2.25^{+4.37}_{-0.99}$ (FPMA) $2.02^{+21.4}_{-1.13}$ (FPMB)	$1.74^{+7.54}_{-0.44}$ (FPMA) $1.67^{+1.26}_{-0.42}$ (FPMB)	$1.39^{+0.36}_{-0.26}$	$1.62^{+0.49}_{-0.35}$	$1.21^{+0.34}_{-0.24}$
Nthcomp(1)	Γ	$1.54^{+0.01}_{-0.01}$ (FPMA) $1.54^{+0.01}_{-0.01}$ (FPMB)	$1.49^{+0.03}_{-0.04}$ (FPMA) $1.49^{+0.02}_{-0.08}$ (FPMB)	$1.46^{+0.01}_{-0.01}$	$1.41^{+0.03}_{-0.04}$	...
	kT_e (keV)	118^{+29}_{-19}	115^{+38}_{-29}	126^{+38}_{-7}	149^{+79}_{-33}	...
relxilllpCp(1) (lower reflection)	Γ	...	...	...	...	$1.38^{+0.01}_{-0.01}$
	kT_e (keV)	...	...	...	...	150^{+9}_{-7}
	h (R_g)	<2.8	$7.41^{+1.94}_{-1.93}$	$4.1^{+0.7}_{-1.8}$	$3.2^{+0.4}_{-0.5}$	$2.8^{+0.8}_{-0.5}$
	θ (°)	29^{+2}_{-8}	25^{+8}_{-2}	27^{+8}_{-10}	35^{+7}_{-9}	30^f
	R_{in} (R_g)	$6.9^{+0.9}_{-1.0}$	$5.4^{+1.5}_{-1.5}$	$2.5^{+1.2}_{-1.0}$	$4.2^{+1.0}_{-0.9}$	1.2^f
	$\log\xi$ (log[erg cm s^{-1}])	$3.9^{+0.2}_{-0.1}$	$3.38^{+0.04}_{-0.03}$	$3.69^{+0.03}_{-0.22}$	$3.68^{+0.03}_{-0.13}$	$4.21^{+0.01}_{-0.01}$
	A_{Fe} ($A_{Fe,\odot}$)	$4.4^{+1.3}_{-0.5}$	$5.0^{+0.3}_{-0.2}$	10.0^p	10.0^p	10.0^p
	$\mathcal{R}$	0.54	1.21	1.93	1.30	2.42
	norm	1.96 (FPMA) 1.70 (FPMB)	0.09 (FPMA) 0.08 (FPMB)	0.05	0.12	0.16
xillverCp	$\log\xi$ (log[erg cm s^{-1}])	$2.5^{+0.2}_{-0.1}$	$2.4^{+0.1}_{-0.2}$	4.70^p	4.70^p	...
	norm ($\times 10^{-2}$)	1.4	0.4	2.36	1.16	...
Nthcomp(2)	Γ	...	$1.66^{+0.02}_{-0.02}$	...	$1.57^{+0.01}_{-0.05}$	...
	kT_e (keV)	...	$14.0^{+2.1}_{-1.7}$	...	$18.4^{+3.6}_{-3.2}$	...
	norm	...	2.17	...	0.40	...
relxilllpCp(2) (upper reflection)	h (R_g)	...	...	...	...	$5.5^{+2.3}_{-1.2}$
	Γ	...	...	...	...	$1.44^{+0.01}_{-0.01}$
	kT_e (keV)	...	...	...	...	$22.9^{+7.4}_{-4.3}$
	$\log\xi$ (log[erg cm s^{-1}])	...	...	...	...	$3.62^{+0.09}_{-0.07}$
	$\mathcal{R}$	...	...	...	...	1.92
	norm	...	...	...	...	0.01
χ^2/dof		715.1/670	666.1/667	872.0/814	856.8/811	861.4/818
	C_{LAXPC}	...	...	1.95	1.95	1.93
	C_{CZTI}	...	...	1.94	1.94	1.93
	C_{FPMB}	0.96	0.96	...	...	...
Unabsorbed flux	3.0–70.0 keV	8.9	8.9	7.8	7.8	7.8

Notes. T_{in}: Temperature of the inner disc; norm: Normalization of the corresponding spectral parameter; Γ: Asymptotic power-law photon index; T_e: Electron temperature of the corona, determining the high energy rollover; h: Height of the comptonizing lamp-post corona above the black hole; θ: Inclination of the inner disc; R_{in}: Inner disc radius (in units of R_g); ξ: Ionization parameter of the accretion disc, defined as $\xi = L/nR^2$, with L, n, R being the ionizing luminosity, gas density, and the distance to the ionized source, respectively; A_{Fe}: Iron abundance, in the units of solar abundance; $\mathcal{R}$: Reflection fraction; C_{LAXPC}: the flux normalization constant for LAXPC (determined by multiplicative 'constant' parameter in the spectral models) is estimated with respect to the SXT flux. Similarly, we have denoted C_{CZTI} for CZTI flux normalization constant with respect to the SXT flux, and C_{FPMB} for FPMB flux normalization constant with respect to the FPMA flux.

act solely as reflection, both reflecting the NTHCOMP component. The seed temperature of the NTHCOMP is tied to the DISKBB T_{in}, the kT_e and Γ of the NTHCOMP, RELXILLLPCP, and XILLVERCP are tied to each other. The A_{Fe} and θ, of the XILLVERCP are tied to that of RELXILLLPCP component, while its ξ is allowed to vary freely. Basically, this model comprises of a single Comptonization continuum being reflected from the disc by two different reflection components, one blurred and the other unblurred.

(ii) TBabs× (diskbb+Nthcomp(1)+relxilllpCp(1) +xillverCp+Nthcomp(2)): This makes the M2 model in Table 2. Here, the NTHCOMP(1) acts as the hard/primary continuum, and the RELXILLLPCP reflects the NTHCOMP(1) component. The seed temperature of the NTHCOMP(1) is tied to the DISKBB T_{in}, the kT_e and Γ of the NTHCOMP and RELXILLLPCP are tied to each other. The NTHCOMP(2) component denotes the second, soft Comptonization component; reflected by the XILLVERCP component. The seed tem-

perature of the NTHCOMP(2) is tied to the DISKBB T_{in}, and the kT_e and Γ of the XILLVERCP are tied to that of the NTHCOMP(2) component. Just like in M1, the A_{Fe} and θ, of the XILLVERCP are tied to that of RELXILLLPCP component, while its ξ is allowed to vary freely. More crucially, the kT_e and Γ of the two Comptonization components are not tied to each other. Essentially, this model comprises of two Comptonization continuum being reflected from the disc by two different reflection components, one blurred and the other unblurred, having different temperatures (and potentially two different lamp-post heights). This better mimics a realistic corona, allowing for a temperature structure.

To make a reasonable comparison with the *NuSTAR* spectral fit by Buisson et al. (2019), we allow the DISKBB T_{in} and normalization, as well as the spectral index and normalization of the intrinsic continuum to vary freely between FPMA and FPMB. This takes care of the slight calibration differences between the two modules. We find that apart from the DISKBB normalization, the typical difference between the two modules in the other quantities are less than the stated calibration level (Madsen et al. 2015). The introduction of the reflection models vastly improves the goodness of fit. For model M1, the χ^2/dof is found to be 715.1/670. The innermost accretion disc temperature is observed to be $0.44^{+0.08}_{-0.07}$ keV, which is lower than the values reported by Buisson et al. (2019). However, we have to keep in mind that *NuSTAR* extends only up to 3.0 keV in lower energy side, and hence is not extremely suitable for accurate estimation of the accretion disc parameters on its own. Most of the other parameters, viz. Γ, R_{in}, $\log \xi$, A_{Fe} are found to be consistent with the parameters in RELXILLLPCP(1) model fit of epoch 3 spectra in Buisson et al. (2019). The values of Γ are consistent with hard state spectra of black hole X-ray binaries (Remillard & McClintock 2006). Inner disc radius (R_{in}, of $6.9^{+0.9}_{-1.0}R_g$) extending very close to the ISCO and supersolar abundances (A_{Fe} of $4.4^{+1.3}_{-0.5}$ time solar) are also observed. The proximity of the inner radius of the disc to the ISCO is consistent with Kara et al. (2019), Buisson et al. (2019). The non-zero ionization parameter ($\log \xi = 2.5^{+0.2}_{-0.1}$ log[erg.cm/s]) of the XILLVERCP indicates the presence of an ionized distant reflection component. However, the lamp-post height is found to be pegged near the lowermost allowable limit. The inclination angle is found to be 29^{+2}_{-8} degrees. Additionally, we observe a higher corona temperature (118^{+29}_{-19} keV) than the previously reported values. The best-fitting parameter values are presented in the first column of Table 2.

Addition of the second Comptonization component improves the best fit significantly. If the kT_e of the additional NTHCOMP is tied to that of the original RELXILLLPCP component, the fit results in a χ^2/dof of 688.8/668. The common temperature of the corona is found to be 38^{+3}_{-2} keV. This value is similar to that obtained by Buisson et al. (2019), the implication of which is discussed later in this section and section 4. Now, if we untie the two kT_e components (thus forming model M2), the χ^2/dof becomes 666.1/667. The addition of the three free parameters change the best-fitting values. All the disc reflection parameters, including the lamp-post height ($7.41^{+1.94}_{-1.93}R_g$), are found to be more or less consistent with the epoch 3 results from Buisson et al. (2019). The additional Comptonization component is found to be at a much lower kT_e value of $14.0^{+2.1}_{-1.7}$ keV, as compared to 115^{+38}_{-29} keV of the primary Comptonization component. The best-fitting parameter values can be found in the second column in Table 2. This segregation of the temperatures of the two coronal components hints towards the existence of an inhomogeneous corona. When the temperatures of the two components are tied, we get an average temperature of $\sim$38 keV, which Buisson et al. (2019) found. An *F*-test between the fits with M1 and M2 model yields a very low false-positive probability of 2.9×10^{-10}, further solidifying the importance of the second Comptonization component for obtaining a good fit. A detailed representation of the different spectral components can be found in Fig. 4 and the *NuSTAR* residual with M2 model fit is presented in the bottom panel in Fig. 3.

Similar to the *NuSTAR* spectral fits, we model the joint SXT+LAXPC+CZTI spectra. The broader energy range of 1.3–120.0 keV gives us a better handle over the disc parameters and high energy rollover, although the poorer spectral resolution around the iron lines gives a less reliable measurement of the reflection parameters. The best-fitting parameters from M1 model fit are found to be a little different than the contemporaneous *NuSTAR* fit. The inner disc temperature ($0.33^{+0.01}_{-0.01}$ keV) is found to be somewhat higher than the value reported in Mudambi et al. (2020), and close to the is typical T_{in} values for the hard spectral state in black hole X-ray binaries (e.g. Wilkinson & Uttley 2009; Wang-Ji et al. 2018). The spectral index $1.46^{+0.01}_{-0.01}$ is found to be somewhat lower than the *NuSTAR* values. The corona temperature (126^{+38}_{-7} keV) and ionization parameter ($\log \xi = 3.69^{+0.03}_{-0.22}$ log[erg cm s^{-1}]) are found to be close to the *NuSTAR* fit values. The lamp-post height ($4.1^{+0.7}_{-1.8}R_g$) is also found to be consistent with the Buisson et al. (2019) value. The *AstroSat* fit is also observed to prefer a closer inner disc. However, the iron abundance and the XILLVERCP ionization parameter are pegged near the maximum allowed values. The maximality of the XILLVERCP ionization parameter is most likely due to the limited spectral capability of LAXPC (more specifically, in LAXPC20), as discussed in Section 4. Additionally, the LAXPC residual shows a peak at $\sim$36 keV, which is not present in CZTI residual, indicating an instrumental origin. The feature can be attributed to Xenon K-edge and can be taken care of with the inclusion of a GAUSSIAN component (Sridhar et al. 2019). We found that a GAUSSIAN component of line energy $\sim$35.9 keV and width σ $\sim$0.8 keV sufficiently takes care of the feature. The resultant M1 model fit yields a χ^2/dof of 872.0/814.

Similar to *NuSTAR* M2 model fit, we add a second NTHCOMP component to the *AstroSat* M1 fit. The resultant M2 model fit yields a much better χ^2/dof of 856.8/8111. The best-fitting *AstroSat* values are noted to be closer to the *NuSTAR* values for M2 model fit. The DISKBB temperature remains almost unchanged. The lamp-post height ($3.18^{+0.38}_{-0.47}R_g$) is found to be consistent with Kara et al. (2019). Similar to *NuSTAR* , the fit with the M2 model results in a much lower value of the kT_e of the second Comptonization ($18.4^{+3.6}_{-3.2}$ keV), as opposed to the higher kT_e value (149^{+79}_{-33} keV) of the primary Comptonization component. The iron abundance and the XILLVERCP ionization parameter are still found to be pegged at the upper limit. The spectral index of the second NTHCOMP is found to be steeper ($1.57^{+0.01}_{-0.05}$) than the intrinsic Comptonization component ($1.41^{+0.03}_{-0.04}$). The inner disc radius ($4.2^{+1.0}_{-0.9}R_{ISCO}$) also becomes comparable to the *NuSTAR* best-fitting value. The best-fitting parameter values for M1 and M2 fit are reported in the 3rd and 4th column in Table 2. The spectra and the residuals can be found in Fig. 5. The high cross-normalization factors between SXT and LAXPC/CZTI can be attributed to the small extraction area for SXT (explained in greater detail in appendix A). To further probe the effect of LAXPC on the significance of the second Comptonization component, we fit the SXT+CZTI spectra between 1.3–5.0 and 40.0–120.0 keV with TBABS×(DISKBB+NTHCOMP) and TBABS×(DISKBB+NTHCOMP+NTHCOMP) models. The former fit results in a χ^2/dof of 1165.2/741, while the latter gives a χ^2/dof of 824.8/738. This further establishes the importance of the second Comptonization component.
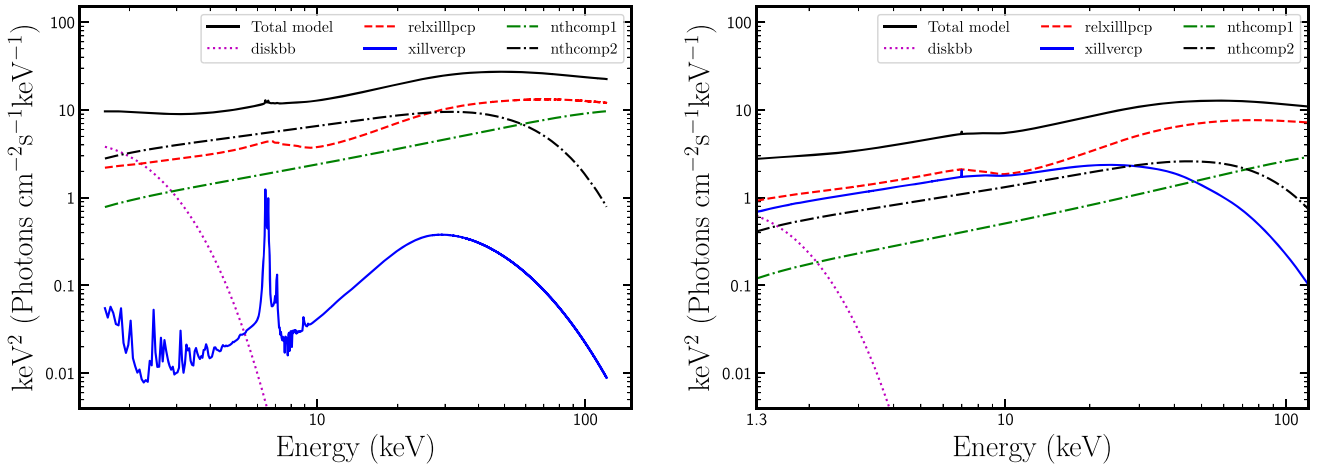
Figure 4. Best-fitting M2 model for *NuSTAR* (left-hand panel) and *AstroSat* (right-hand panel). The dotted magenta curve corresponds to the multicolour disc component. The dashed red curves and solid blue curves mark the RELXILLLPCP and XILLVERCP components, respectively. The intrinsic NTHCOMP continua are represented by the green dash-dotted curves. The black dash-dotted curves indicate the second NTHCOMP Comptonization components, with lower rollover energy. The spectral components are detailed in section 3.2.2, and the implications discussed in section 4.
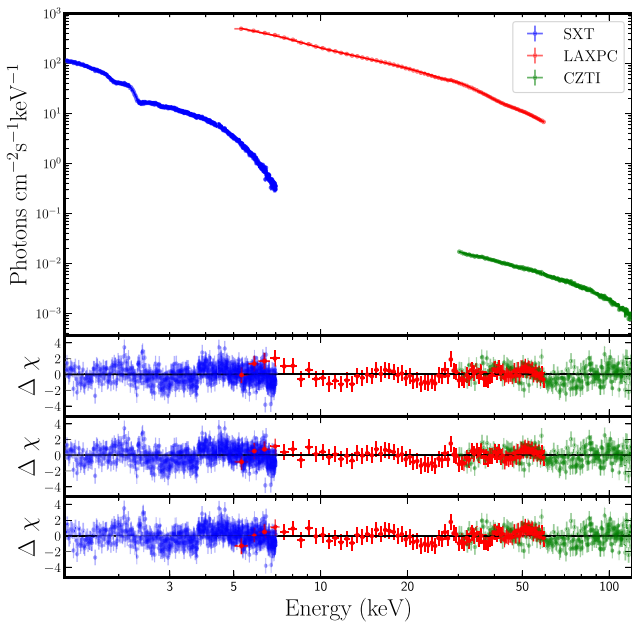
Figure 5. Results of 1.3–120 keV *AstroSat* spectral fit of MAXI J1820+070 (see sections 3.2.2, 4 for further details). Top panel: the *AstroSat* spectra. The blue, red, and green points indicate SXT (1.3–7.0 keV), LAXPC (5–60 keV), and CZTI (30–120 keV) data, respectively. The spectra are fitted with M2 model here. The difference in normalization between SXT and the rest of the instruments can be attributed to small region of extraction we used to avoid pile-up (detailed in section A). Second panel: Residuals from the M1 model fit. Third panel: Residuals from M2 model fit. Bottom panel: Residuals from M3 model fit.

Finally, for a closer parallel to the *AstroSat* data with the published *NuSTAR* fits, we adopt a similar model to Buisson et al. (2019), involving a DISKBB and two RELXILLLPCP components (denoted as RELXILLLPCP(1) for the reflection component with lower height, and RELXILLLPCP(2) for the higher corona). All the continuum parameters are allowed to vary freely. For simplicity, the inner disc radius is fixed at the ISCO. Thus, this model

(M3: TBABS×(DISKBB+RELXILLLPCP(1)+RELXILLLPCP(2))) has two Comptonization components at different heights, which are reflected from the inner disc. The resulting fit (model M3 in Table 2) can be compared to M2 model fit, with a χ^2/dof of 861.4/818. The inclination angle is fixed at 30°, as allowing it to freely vary results in an unconstrained inclination value. The corona temperature shows a clear segregation, with a much higher temperature (150^{+9}_{-7} keV) for the corona closer to the black hole and a much lower temperature ($22.9^{+7.4}_{-4.3}$ keV) for the corona component further away. The temperature of the colder corona is somewhat consistent wih *NuSTAR* and *AstroSat* M2 best-fitting temperatures of the second Comptonization component. The hotter corona (height of $2.8^{+0.8}_{-0.5} R_g$) component is also found to have higher ionization parameter than the colder corona (height of $5.5^{+2.3}_{-1.2} R_g$) component. Note that, although the temperature structure is prominent, the segregation of lamp-post heights is not as pronounced as reported by Buisson et al. (2019).

3.2.3 Estimation of mass of the black hole

The inner accretion disc radius in a black hole LMXB can be measured either from fitting the disc or from modelling the disc reflection. Assuming the inner radii deduced from the DISKBB and RELXILLLPCP components to be the same, we can derive the mass of the black hole (M_{BH}) from equation (3) in Wang et al. (2018). We use a correction factor of 1.2 (Kubota et al. 1998), accounting for the spectral hardening (Shimura & Takahara 1995) and the fact that the disc temperature does not peak at the inner radius (Makishima et al. 2000, see also equation 2 and the corresponding discussion in Reynolds & Miller 2013).

Using our best-fitting values of R_{in} and DISKBB normalization from a fit with the *AstroSat* model M2, as well as considering a distance estimate from Gandhi et al. (2019), we get the mass of the black hole in MAXI J1820+070 to be 6.7–13.9 $M_\odot$. This mass estimate from our spectral model is consistent with the estimates from dynamical mass measurement from Torres et al. (2019) (7–8 $M_\odot$) and radio parallax measurement by Atri et al. (2020) ($9.2 \pm 1.3 M_\odot$). Additionally, this mass estimate from the hard state spectra is also consistent with the mass value derived from soft state spectra (Fabian et al. 2020).

4 DISCUSSIONS

In this paper, we report the results of broad-band spectral analysis of 2018 hard state data of the transient black hole X-ray binary MAXI J1820+070 using all three pointing X-ray instruments (SXT, LAXPC, and CZTI) on board *AstroSat*, as well as the nearest (both in time and in HID) available *NuSTAR* data. *NuSTAR* and *AstroSat* are the two most prominent currently active broad-band X-ray satellites. While the *NuSTAR* data provides us with an opportunity to investigate the reflection features due to its superior energy resolution, the *AstroSat* data provides us a better handle over some other continuum parameters due to its much broader energy coverage between 1.3 and 120.0 keV. Thus, studying the source systematically in similar, contemporaneous states with the same models utilizing two of the most prominent broad-band instruments with such complementary capabilities, we derive conclusions that are more general and reliable. While the *NuSTAR* spectra are explored in great detail by Buisson et al. (2019), they tied the two coronal temperature. We show, in section 3.2.2, that this leads to a similar temperature even with our different model implementation. We further show that a much more general assumption of untied temperatures between the two coronal components leads to a better fit and segregation of the two temperatures. Similarly, the *AstroSat* spectrum has been presented in Mudambi et al. (2020). However, it is used to get a rough understanding of the spectrum to help in their main aim of spectrotiming study. That apart, their spectra did not include CZTI, a better understanding of SXT pile-up, and not a very good fit even with 3 per cent systematics (as opposed to the recommended 2 per cent we have used). The DISKBB normalization they derived, would imply to a black hole mass of 22–$26\,M_\odot$, leading to inconsistent results. This motivated us to further explore the *AstroSat* data, with all three pointing X-ray instruments, in much greater detail.

The broad-band spectra contains presence of soft excess, broad, and narrow iron line complex and a Compton hump. The resultant spectrum is well fitted with the combination of a multicolour disc blackbody, a corona with a lamp-post geometry in the form of self-consistent, relativistic reflection model RELXILLLPCP (which contains an intrinsic thermal Comptonization continuum), and a distant, unblurred reflection component in the form of XILLVERCP. The resultant model, M1, is detailed in Section 3.2.2 and Table 2. From the best-fitting *NuSTAR* spectra, we find the parameter values to be largely consistent with the previously reported values by Buisson et al. (2019) (epoch 3). The supersolar iron abundance of $4.4^{+1.3}_{-0.5}$ (relative to solar values) is also found to be consistent with the previous results. Similar overabundance of iron has been reported in various X-ray binaries (e.g. Degenaar et al. 2017; García et al. 2018; Tomsick et al. 2018). The spectral index of the intrinsic NTHCOMP is found to be 1.54–1.55, typical of black hole X-ray binaries in the hard state. The distant reflection component is found to be ionized. The DISKBB T_{in} is found to be $\sim$0.42–0.45 keV, which is lower than the previously reported value by Buisson et al. (2019). It is to be noted, however, that *NuSTAR* less reliable for the measurement of the DISKBB temperature and normalization. Additionally, the *NuSTAR* data fit with the M1 model reveals a higher corona temperature (118^{+29}_{-19} keV) than previously reported. For the spectral characterization of *AstroSat* data, we jointly fit the SXT (corrected for pile-up and appropriately gain shifted), LAXPC (LAXPC20), and CZTI data, utilizing the full broad-band capability of *AstroSat* between 1.3 and 120.0 keV. The *AstroSat* best fit with M1 model indicates a lower but better constrained DISKBB T_{in} of $0.33^{+0.01}_{-0.01}$ keV, a similar corona temperature and ionization parameter, and a somewhat lower spectral index.

We also explore the possibility of a two-component corona through the addition of an external NTHCOMP to our existing model. This implementation is similar in nature to the RELXILLLPCP+RELXILLLPCP scenario considered in Buisson et al. (2019), but has some key differences. Both the ionization parameter and the electron temperature of the two Comptonization components (the intrinsic NTHCOMP continuum of the RELXILLLPCP model and the added NTHCOMP) are kept free and independent of each other. This gives us a more consistent and general picture, as the two components of the corona might have different physical properties. The inclusion of this additional Comptonization component (the M2 model) vastly improves the goodness of fit for both *NuSTAR* and *AstroSat* data. In case of *NuSTAR*, tying up the temperature of the two coronal components leads to a kT_e of 38^{+3}_{-2} keV, consistent with Buisson et al. (2019). Untying the two temperatures and letting both vary freely; leads to a much better χ^2/dof than the previously reported models. The DISKBB T_{in} is almost unaffected by the inclusion of this added component, and the other best-fitting parameters are broadly consistent between *NuSTAR* and *AstroSat*. For both *NuSTAR* and *AstroSat*, the height of the lamp-post corona is found to be consistent with Kara et al. (2019). Letting both the corona temperatures free, leads to a segregation of temperatures for both *NuSTAR* and *AstroSat*. While the temperature of the primary Comptonization component is found to be 115^{+38}_{-29} and 149^{+79}_{-33} keV, the kT_e of the second Comptonization component is found to be $14.0^{+2.1}_{-1.7}$ and $18.4^{+3.6}_{-3.2}$ keV for *NuSTAR* and *AstroSat* data, respectively. This difference in corona temperatures can be interpreted as originating from different distances from the black hole. The high energy corona is much closer to the black hole, has a higher electron temperature, and contributes to the broad iron line through blurred reflection; while the low energy corona is further away, has much lesser electron temperature, and contributes to the narrow core of the iron line complex. Similar interpretation of inhomogeneous corona has been used for Cyg X-1 (Yamada et al. 2013; Basak et al. 2017). This idea is further reinforced by the implementation of our M3 model in Table 2, where for *AstroSat* data we used a model almost similar to Buisson et al. (2019), with both the corona reflecting for a disc extending upto the ISCO and the continuum parameters of the two corona allowed to vary freely. This leads to a separation in both temperature and (to a certain extent) height, with the corona further away (RELXILLLPCP(2)) having lower ionization and temperature than the corona closer to the back hole (RELXILLLPCP(1)). Note that this interpretation, though a little different, is not inconsistent with the contracting corona scenario (Kara et al. 2019); it just assigns a more realistic temperature structure to the corona. This also shows that tying up the temperatures of the higher and lower temperature corona leads to an average temperature, similar to the one found by Buisson et al. (2019).

A few points are to be noted about the fits described in our work. First of all, by setting the RELXILLLPCP and XILLVERCP refl_frac<0 (thereby including only the reflected flux from the respective components), we attempt to avoid the possibility of the second reflection component adding significantly to the continuum (and hence mimicking the spectra for a second corona temperature), rather than only fitting the reflection features (iron line, Compton hump etc.). The similarity in the best-fitting parameters for *NuSTAR* and *AstroSat*, and the likelihood of the second Comptonization with a similar temperature for both the instruments provide a further credence to our claim of a multitemperature corona. That apart, the M3 model fit of *AstroSat* data provides further support that the two different temperatures can be attributed to different corona heights. Nevertheless, the alternate scenario (only one temperature

and second reflection component adding to the continuum) cannot be entirely ruled out.

As XILLVERCP corresponds to a corona situated farther away, this component should be less ionized than the RELXILLLPCP component. This is what we find for *NuSTAR* fits (see Table 2). However, the XILLVERCP ionization parameter, for *AstroSat* fits, is pegged to a maximal value, and is higher than the best-fitting value of the RELXILLLPCP ionization parameter (see Table 2). This higher value could be because *AstroSat* (LAXPC20, in particular) cannot adequately describe the narrow features of XILLVERCP (see Fig. 4) due to a limited spectral capability. However, the XILLVERCP component is necessary even for *AstroSat* fits. We conclude this, because, while the χ^2/dof is 856.8/811 for the model M2, it is 885.1/814 if XILLVERCP is excluded from M2. Note that, if we force a lower value of the XILLVERCP ionization parameter, by tying it to the RELXILLLPCP ionization parameter for the M2 model of *AstroSat* fitting, the contribution of the XILLVERCP component becomes negligible, and the fit is much worse with χ^2/dof = 886.4/813. Nevertheless, the best-fitting parameter values (e.g. DISKBB $T_{in} = 0.29^{+0.01}_{-0.01}$ keV) for this modified M2 model are overall consistent with those for the M2 model for *AstroSat* fitting. Moreover, the fits of both *AstroSat* and *NuSTAR* spectra with the M2 model give a similar conclusion, e.g. a temperature structure of the corona. These give confidence to our results, and we list the best-fitting parameter values for the *AstroSat* M2 model fit in Table 2, although *AstroSat* cannot adequately model the XILLVERCP component.

The R_{in} for both *NuSTAR* and *AstroSat* are found to be of similar values ($5.4^{+1.5}_{-1.5} R_g$ for *NuSTAR*, and $4.2^{+1.0}_{-0.9} R_g$ for *AstroSat* for M2 model fit; see Table 2). For a maximally spinning black hole, this would place the inner edge of the accretion disc at $2.7–5.6 R_{ISCO}$ (R_{ISCO}: radius of the innermost stable circular orbit). However, this does not necessarily imply a truncated disc, as R_{in} and a are degenerate and we fix the dimensionless spin parameter (a) to 0.998, only to simplify a stable fitting process (section 3.2.2). Note that R_{ISCO} is determined by the black hole spin, and it monotonically increases from $1.24R_g$ for an extremely prograde spinning black hole to $9.0R_g$ for an extremely retrograde spinning black hole. The alternate scenario of a low black hole spin with a disc extending all the way down to ISCO, is equally likely, and the spectral fitting alone may be insufficient to distinguish between different a-values. In fact, the almost unchanging R_{in} from Kara et al. (2019) and the consistency of best-fitting R_{in} throughout the eight epoch in Buisson et al. (2019) imply that R_{in} does not vary much throughout the outburst. Furthermore, the soft state spectral fitting by Fabian et al. (2020) supports a spin value between -0.5 and $+0.5$. Both these evidences indicate that MAXI J1820+070 may contain a low spin black hole, with the disc extending to ISCO. To test if our best-fitting parameter values allow this possibility, we fix the R_{in} to the ISCO radius, make the spin parameter a free, fix the inclination at $30°$, and freeze all the other parameters (except the normalizations) to their best-fitting values in the M2 model fit of *NuSTAR* data. This results in an acceptable fit, with a χ^2 of 672.0 for 678 degrees of freedom. The corresponding best-fitting spin parameter is $0.48^{+0.25}_{-0.26}$, which is consistent with Fabian et al. (2020).

Finally, assuming the same inner disc radius between the DISKBB and RELXILLLPCP, we calculate the mass of the black hole to be 6.7–13.9 $M_\odot$, consistent with previously reported values. This is the first time the mass of this black hole has been calculated from the hard state spectra in such a way. It is to be noted that most studies deriving the colour-correction factor have involved BHXBs predominantly in soft state (see Merloni, Fabian & Ross 2000; Reynolds & Miller 2013, for exceptions), and a higher value might be warranted in hard states

(Dunn et al. 2011; Reynolds & Miller 2013; Davis & El-Abd 2019). The consistency of the black hole mass estimate through this method with the other values, however, can provide a justification towards a disc origin of the thermal emission (as opposed to a reflection origin). This is further corroborated by Fabian et al. (2020).

From our best-fitting model (M2), we find the unabsorbed 0.1–500 keV flux to be $1.64–1.69 \times 10^{-7}$ erg cm^{-2} s^{-1} for the *NuSTAR* data and $1.62–1.64 \times 10^{-7}$ erg cm^{-2} s^{-1} for the *AstroSat* data. This implies a 0.1–500 keV luminosity of $L_{0.1–500\,keV} \sim 2.32–2.42 \times 10^{38}$ erg s^{-1}. This implies that the black hole in MAXI J1820+070 is accreting at 13–29 per cent L_{Edd}.

To summarize, through systematic investigation of contemporaneous *AstroSat* and *NuSTAR* data in similar states and with similar models, we have characterized the broad-band X-ray spectra of the transient black hole X-ray binary MAXI J1820+070 in the hard state (2018 March) during its 2018 outburst. The *NuSTAR* best-fitting parameters are found to be largely consistent with the values reported in the literature. We also fully utilize the broad-band capability of all the pointing X-ray instruments on board *AstroSat*, through consistent spectral analysis in 1.3–120.0 keV energy range. Though there are some quantitative differences of the best-fitting parameters between *NuSTAR* and *AstroSat*, the broad conclusions are consistent with each other. The inclusion of *AstroSat* data complements the *NuSTAR* data, as *NuSTAR* spectral fit gives us a better estimate of the reflection parameters, while *AstroSat* data provides superior estimates of disc temperature, normalization, and the high energy rollover of the corona. We utilize this potential to also investigate the possibility of an inhomogeneous corona through the implementation of a double Comptonization model, which leads to better goodness of fit for both *NuSTAR* and *AstroSat* data. The consistency of the low energy Comptonization component for independent observations with different instruments in a similar state (with *AstroSat* covering a broader energy range) establishes the significance of our results.

DATA AVAILABILITY

The observational data used in this paper are publicly available at NASA's High Energy Astrophysics Science Archive Research Center (HEASARC; https://heasarc.gsfc.nasa.gov/) and ISRO's Science Data Archive for AstroSat Mission (https://astrobrowse.issdc.gov.

in/astro_archive/archive/Home.jsp), and references are mentioned. Any additional information will be available upon reasonable request.

REFERENCES

Agrawal P. C., 2006, Adv. Space Res., 38, 2989
Arnaud K. A., 1996, in Jacoby G., Barnes J., eds, XSPEC: The First Ten Years, Astronomical Data Analysis Software and Systems V , ASP Conf. Ser., Vol. 101,p. 17
Atri P. et al., 2020, MNRAS, 493, L81
Baglio M. C., Russell D. M., Lewis F., 2018, Astron. Telegram, 11418, 1
Bahramian A., Strader J., Dage K., 2018, Astron. Telegram, 11424, 1
Basak R., Zdziarski A. A., Parker M., Islam N., 2017, MNRAS, 472, 4220
Belloni T., Klein-Wolt M., Méndez M., van der Klis M., van Paradijs J., 2000, A&A, 355, 271
Belloni T., Homan J., Casella P., van der Klis M., Nespoli E., Lewin W. H. G., Miller J. M., Méndez M., 2005, A&A, 440, 207
Bright J., Fender R., Motta S., 2018, Astron. Telegram, 11420, 1
Buisson D. J. K. et al., 2019, MNRAS, 490, 1350
Casella P., Vincentelli F., O'Brien K., Testa V., Maccarone T. J., Uttley P., Fender R., Russell D. M., 2018, Astron. Telegram, 11451, 1
Chauvin M. et al., 2018, Nat. Astron., 2, 652
Dauser T., Garcia J., Parker M. L., Fabian A. C., Wilms J., 2014, MNRAS, 444, L100
Davis S. W., El-Abd S., 2019, ApJ, 874, 23
Degenaar N., Pinto C., Miller J. M., Wijnands R., Altamirano D., Paerels F., Fabian A. C., Chakrabarty D., 2017, MNRAS, 464, 398
Del Santo M., Segreto A., 2018, Astron. Telegram, 11427, 1
Denisenko D., 2018, Astron. Telegram, 11400, 1
Done C., Gierliński M., Kubota A., 2007, A&A Rev., 15, 1
Dunn R. J. H., Fender R. P., Körding E. G., Belloni T., Merloni A., 2011, MNRAS, 411, 337
Fabian A. C., 2016, Astron. Nachr., 337, 375
Fabian A. C. et al., 2020, MNRAS, 493, 5389
Fender R. P., Homan J., Belloni T. M., 2009, MNRAS, 396, 1370
Frank J., King A., Raine D. J., 2002, Accretion Power in Astrophysics, 3rd edn., Cambridge University Press, Cambridge, UK
Gandhi P., Paice J. A., Littlefair S. P., Dhillon V. S., Chote P., Marsh T. R., 2018, Astron.Telegram, 11437, 1
Gandhi P., Rao A., Johnson M. A. C., Paice J. A., Maccarone T. J., 2019, MNRAS, 485, 2642
García J., Kallman T. R., 2010, ApJ, 718, 695
García J. et al., 2014, ApJ, 782, 76
García J. A. et al., 2018, ApJ, 864, 25
Garnavich P., Littlefield C., 2018, Astron. Telegram, 11425, 1
Harrison F. A. et al., 2013, ApJ, 770, 103
Homan J., Belloni T., 2005, Ap&SS, 300, 107
Homan J., Wijnands R., van der Klis M., Belloni T., van Paradijs J., Klein-Wolt M., Fender R., Méndez M., 2001, ApJS, 132, 377
Houck J. C., Denicola L. A., 2000, in Manset N., Veillet C., Crabtree D., eds, ISIS: An Interactive Spectral Interpretation System for High Resolution X-Ray Spectroscopy, Vol. 216, Astronomical Data Analysis Software and Systems IX, ASP Conf. Proc., p. 591
Kara E. et al., 2019, Nature, 565, 198
Kawamuro T. et al., 2018, Astron. Telegram, 11399, 1
Kennea J. A., 2018, Astron. Telegram, 11406, 1
Kubota A., Tanaka Y., Makishima K., Ueda Y., Dotani T., Inoue H., Yamaoka K., 1998, PASJ, 50, 667
Littlefield C., 2018, Astron. Telegram, 11421, 1
Madsen K. K. et al., 2015, ApJS, 220, 8
Makishima K., Maejima Y., Mitsuda K., Bradt H. V., Remillard R. A.,Tuohy I. R., Hoshi R., Nakagawa M. , 1986, ApJ, 308, 635
Makishima K. et al., 2000, ApJ, 535, 632
Mandal A. K., Singh A., Stalin C. S., Chandra S., Gandhi P., 2018, Astron. Telegram, 11458, 1
Marcotulli L. et al., 2017, ApJ, 839, 96
Matsuoka M. et al., 2009, PASJ, 61, 999

Mereminskiy I. A., Grebenev S. A., Molkov S. V., Zaznobin I. A., Khorunzhev G. A., Burenin R. A., Eselevich M. V., 2018, Astron. Telegram, 11488, 1
Merloni A., Fabian A. C., Ross R. R., 2000, MNRAS, 313, 193
Mitsuda K. et al., 1984, PASJ, 36, 741
Motta S., Muñoz-Darias T., Casella P., Belloni T., Homan J., 2011, MNRAS, 418, 2292
Mudambi S. P., Maqbool B., Misra R., Hebbar S., Yadav J. S., Gudennavar S. B. S. G. B., 2020, ApJ, 889, L17
Paice J. A., Gandhi P., Page K., Altamirano D., Court J., Charles P., 2018, Astron. Telegram, 11432, 1
Paice J. A. et al., 2019, MNRAS, 490, L62
Reis R. C., Fabian A. C., Miller J. M., 2010, MNRAS, 402, 836
Remillard R. A., McClintock J. E., 2006, ARA&A, 44, 49
Reynolds C. S., 2014, Space Sci. Rev., 183, 277
Reynolds M. T., Miller J. M., 2013, ApJ, 769, 16
Richmond M., 2018, Astron.Telegram, 11596, 1
Roh J., 2020, American Astronomical Society Meeting Abstracts, 379.02, AAS235 Meeting Abstracts, Bull. Am. Astron. Soc. , Honolulu, HI
Romano P. et al., 2006, A&A, 456, 917
Sako S., Ohsawa R., Ichiki M., Maehara H., Morii M., Tanaka M., 2018, Astron. Telegram, 11426, 1
Shimura T., Takahara F., 1995, ApJ, 445, 780
Singh K. P. et al., 2014, in Takahashi T., den Herder J. W. A., Bautz M., eds Space Telescopes and Instrumentation 2014: Ultraviolet to Gamma Ray, Vol. 9144, Proc. SPIE, Montréal, CA. p. 91441S
Singh K. P. et al., 2016, in den Herder J. W. A., Takahashi T., Bautz M., eds, Space Telescopes and Instrumentation 2016: Ultraviolet to Gamma Ray, Vol. 9905, Proc. SPIE, Edinburgh, UK. p. 99051E
Singh K. P. et al., 2017, J. Astrophys. Astron., 38, 29
Sridhar N., Bhattacharyya S., Chandra S., Antia H. M., 2019, MNRAS, 487, 4221
Tetarenko A. J., Bremer M., Bright J., Sivakoff G. R., Miller-Jones J. C. A., Russell T. D., Jacpot Xrb Collaboration, 2018, Astron. Telegram, 11440, 1
Tomsick J. A. et al., 2018, ApJ, 855, 3
Torres M. A. P., Casares J., Jiménez-Ibarra F., Muñoz-Darias T., Armas Padilla M., Jonker P. G., Heida M., 2019, ApJ, 882, L21
Townsend A. et al., 2018, Astron.Telegram, 11574, 1
Trushkin S. A., Nizhelskij N. A., Tsybulev P. G., Erkenov A., 2018, Astron. Telegram, 11439, 1
Tucker M. A. et al., 2018, ApJ, 867, L9
Uttley P. et al., 2018, Astron. Telegram, 11423, 1
Wang Y., Méndez M., Altamirano D., Court J., Beri A., Cheng Z., 2018, MNRAS, 478, 4837
Wang-Ji J. et al., 2018, ApJ, 855, 61
Wilkinson T., Uttley P., 2009, MNRAS, 397, 666
Wilms J., Allen A., McCray R., 2000, ApJ, 542, 914
Xu Y. et al., 2018, ApJ, 852, L34
Yadav J. S. et al., 2016, ApJ, 833, 27
Yamada S., Makishima K., Done C., Torii S., Noda H., Sakurai S., 2013, PASJ, 65, 80
Yu W., Zhang J., Yan Z., Wang X., Bai J., 2018, Astron. Telegram, 11510, 1
Zdziarski A. A., Johnson W. N., Magdziarz P., 1996, MNRAS, 283, 193
Życki P. T., Done C., Smith D. A., 1999, MNRAS, 309, 561

APPENDIX A: PILE-UP CHECK

The SXT PC mode data for MAXI J1820+070 , taken at a time when the source flux is >1 Crab, is found to be highly piled up. In order to investigate and rectify the pile-up effect, we fit the 1.3–5.0 keV SXT data with a TBABS × (DISKBB+NTHCOMP) model, avoiding the Fe K-α complex. The N_H is fixed to 1.5×10^{21} cm^{-2}, as used in the rest of the work, and the NTHCOMP seed temperature is set at the T_{in} of the DISKBB component. This model is applied to different groups of SXT data, each group differing from previous one by the greater amount of area of the central bright region excluded from the source PSF on the SXT CCD, with the outer edge of the selected annular regions
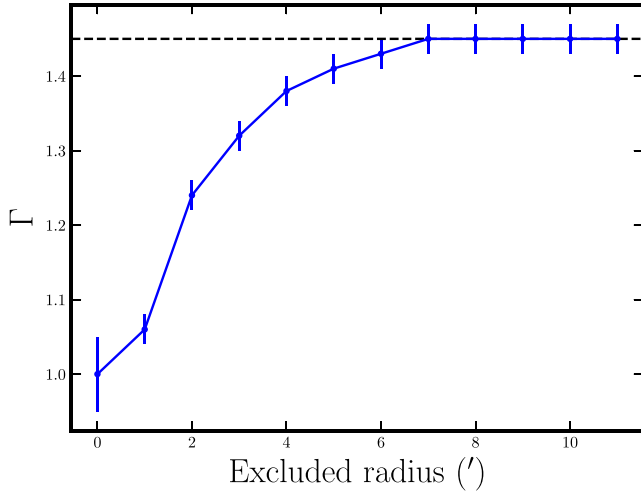
Figure A1. Plot to check the effect of pile-up, following Romano et al. (2006). We use different annular regions in the CCD image, with outer radius fixed at 15 arcmin from the centroid of the PSF and inner radius progressively excluded. Each spectrum is then fitted with a simple model described in Appendix A. The data points show the spectral index (Γ) as a function of the radius of the inner excluded region. We can observe that the spectral index increases and reaches a stable value roughly the same as the M1/M2 fit parameters. We have, therefore, chosen 6 arcmin as the inner radius of the selected source region for the spectral study in section 3.2.2.

fixed at 15 arcmin. Similar to the procedure in Romano et al. (2006), it is noted that the spectra become steeper as more area is excluded until it reaches a stable value (Fig. A1). The radius from the centroid of the PSF, where the spectral index reached a stable value, is chosen to be the inner radius of the annular region. This annular region from 6 to 15 arcmin is used as the source region throughout the rest of the work.
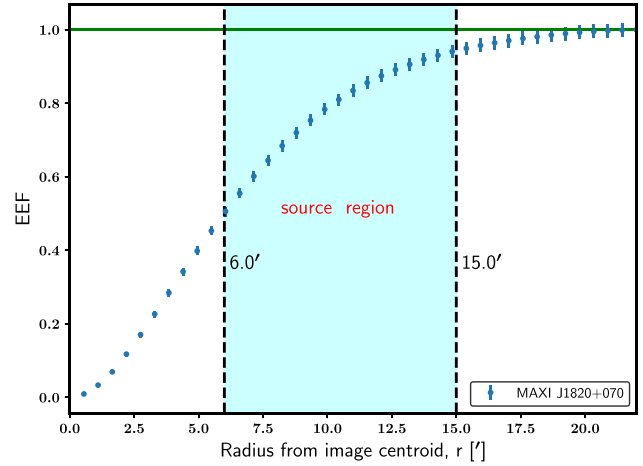

Figure A2. Encircled energy fraction (EEF) of the SXT data of MAXI J1820+070, as a function of distance from the centroid of the PSF. The error bars have been multiplied by a factor of 50 for better representation. The shaded region between 6 and 15 arcmin is the chosen source region for our study.

Fig. A2 shows a plot of the encircled energy fraction (EEF) for SXT data of MAXI J1820+070 . From this plot, we can see that about 44 per cent of photons are encircled within the chosen source region, while a circular region with a radius of 15 arcmin from the centroid of the PSF should contain about 94 per cent of the photons. Thus, the SXT flux is underestimated by a factor of ∼2. This explains the large difference of normalization factor between the SXT and the other two instruments.

This paper has been typeset from a TEX/LATEX file prepared by the author.